Computation of Turbulent Flows and Radiated Sound From Axial Compressor Cascade

Seungbae Lee*, Hooi-Joong Kim
Department of Mechanical Engineering, Inha University, Incheon 402-751, Korea
Jin-Hwa Kim, Seung Jin Song
Department of Mechanical Engineering, Seoul National University, Seoul 151-742, Korea

The losses at off-design points from a compressor cascade occur due to the deviation from a design incidence angle at the inlet of the cascade. The self-noise from the blade cascade at off-design points comes from a separated boundary layer and vortex sheddings. If the incidence angle to the cascade increases, stalling in blades may occur and the noise level increases significantly. This study applied Large-Eddy Simulations (LES) using deductive and deductive dynamic SGS models to low Mach-number, turbulent flow with each incidence angle to the cascade ranging from $-40°$ to $+20°$, and compared numerical predictions with measured data. It was observed that the oscillating separation bubbles attached to the suction surface do not modify wake flows dynamically for cases of negative incidence angles. However, an incidence angle greater than 8° caused a separated vortex near the leading edge to be shed downstream and created stalling. The computed performance parameters such as drag coefficient and total pressure loss coefficient showed good agreement with experimental results. Noise from the cascade of the compressor is summarized as sound generated by a structure interacting with unsteady, turbulent flows. The hybrid method using acoustic analogy was observed to closely predict the measured overall sound powers and directivity patterns at design and off-design points of blade cascade.

Key Words : Cascade, LES, Subgrid-Scale, Aero-Acoustics, Compressor

Nomenclature

C : Chord length
C_0 : Speed of sound
C_D : Drag coefficient
C_L : Lift coefficient
C_{Pt} : Pressure loss coefficient
C_s : Smagorinsky constant
C_x : Blade chord in x-axis direction
G : Gaussian filter function
p : Static pressure
p_t : Total pressure
Re : Reynolds number
S : Domain of surface integration
s : Blade pitch
$\bar{S}_{kl}$: Resolved scale strain rate tensor
T : Stress tensor
U_∞ : Free stream velocity
V : Volume of cell
W : Relative velocity to blade
$\vec{v}$: Velocity vector of (v_1, v_2, v_3) components

Greeks

β : Blade angle
β^* : Blade flow angle
β^*_∞ : Blade mean flow angle
Δ : Filter size
δ : Blade deviation angle
ε : Blade deflection angle

* Corresponding Author,
E-mail : sbaelee@inha.ac.kr
TEL : +82-32-860-7325; **FAX** : +82-32-868-1716
Department of Mechanical Engineering, Inha University, Incheon 402-751, Korea. (Manuscript **Received** August 14, 2002; **Revised** December 9, 2003)

η : Kolmogorov scale
ρ : Density
ν_T : Subgrid-scale eddy viscosity
σ : Solidity
$\bar{\sigma}_{kl}$: Filtered viscous stress tensor
τ_{kl} : Subgrid-scale stress tensor
Ω : Integration domain
ω : Total pressure loss coefficient
ζ : Stagger angle

Subscripts

1 : Conditions at an upstream location of the cascade
2 : Conditions at a downstream location of the cascade
s : Maximum of blade deflection angle
∞ : Free stream or blade averaged conditions

Superscripts

* : Nominal condition
′ : Acoustic field

1. Introduction

In axial compressor study, the two-dimensional cascade model has been often used to increase the accuracy of the prediction and design calculations. Cascade tests and analyses provide the blade-to-blade performance as a function of blade profile, cascade geometry, and operating parameters, finally correcting the differences between the flow in the actual machine and flow through the cascade.

Following the earlier work of Howell (1942) and many others (Johnsen et al., 1965), Lieblien (1965) developed an experimental correlation of extensive cascade data, which can be used as a solid guideline to stall points. The study of fully stalled flow in a two-dimensional cascade has been proven to be of practical engineering significance when one predicts post-stall behavior of a compressor and off-design performance of pumps. The cascade performances at off-design points of large incidence angles have been sought to predict windmilling cranking phase of turbo-engine. Sovran (1959) reported that for conditions when rotating stall occurred, the phenomena closely resemble a Karman vortex street. Yocum and O'Brien (1993) presented flow visualization and time-mean velocity characteristics of stalled flow in a cascade. They suggested that the flow of a larger stagger cascade is more easily diverted around the separation region, resulting in the separated region extending further into the blade passage.

Cornell (1954) calculated the losses and deflection from complete mixing of the jet and the wake by analytically solving for the potential flow through a flat plate cascade. A finite volume approach was attempted by Hah (1985) to solve turbulent flow-fields through a cascade of airfoils at stall conditions. However, changes in performance beyond initial stall and unsteady characteristics were not reported. Although significant progress has been made recently in the turbulent flow solution of the problem, no attempts have been made to predict the unsteady flows within the blade passage and their effects upon mixing of the jet and the wake.

We propose here to use the LES algorithm to provide a more fundamental understanding of separated flow in cascades and to provide performance data for fully stalled flow (Lee and Meecham, 1996). In large-eddy simulations, one calculates directly the large-scale turbulent motions with a relatively coarse time-dependent, three-dimensional computation using the subgrid-scale (SGS) model for the effects of the small-scale motions upon the large scale ones. The LES approach contributes to the quantitative estimation of losses and illumination of fundamental physics at stalled conditions.

Noise caused by stalled flow in a cascade may be considered to be of dipole nature because the dipole source becomes dominant in the separated flow over a surface with appreciable curvature effect. A numerical study of the distant acoustic fields generated by unsteady fluid motion was also performed in this study.

2. Computational Procedure

2.1 Governing equations and model

Development of an LES formulation applicable to a non-orthogonal grid system begins with the

compressible continuity, Navier-Stokes equation in integral form.

$$\frac{\partial}{\partial t}\int_{\Omega}\rho d\Omega+\int_{S}\rho\vec{u}\cdot\vec{n}dS=0 \tag{1}$$

$$\frac{\partial}{\partial t}\int_{\Omega}\rho\vec{u}d\Omega+\int_{S}\rho\vec{u}\vec{u}\cdot\vec{n}dS =\int_{S}T\cdot\vec{n}dS+\int_{\Omega}\rho\vec{b}d\Omega \tag{2}$$

Direct filtering of the continuity equation yields

$$\frac{\partial\bar{u}_i}{\partial x_i}=0 \tag{3}$$

Direct filtering of the momentum equation yields

$$\rho\left[\frac{\partial\bar{u}_i}{\partial t}+\frac{\partial}{\partial x_j}(\bar{u}_i\bar{u}_j)\right]=-\frac{\partial\bar{p}}{\partial x_i}+\frac{\partial\bar{\sigma}_{ij}}{\partial x_j}+\frac{\partial\tau_{ij}}{\partial x_j} \tag{4}$$

where,

$$\tau_{ij}=-\rho(\overline{\bar{u}_i\bar{u}_j}-\bar{u}_i\bar{u}_j+\overline{\bar{u}_iu_j'}+\overline{\bar{u}_iu_j'}+\overline{u_i'u_j'})$$

is called the subgrid-scale stress tensor.

The filtered momentum equation is now solvable if we provide a model for τ_{ij}. The subgrid-scale stress tensor, τ_{ij}, can be decomposed into the subgrid-scale Leonard, Cross, and Reynolds stresses based on spatial filtering. The subgrid-scale stress tensor can be decomposed into the following components: $\tau_{ij}=L_{ij}+C_{ij}+R_{ij}$, defined as $L_{ij}=\overline{\bar{u}_i\bar{u}_j}-\bar{u}_i\bar{u}_j$, $C_{ij}=\overline{u_i'\bar{u}_j}+\overline{\bar{u}_iu_j'}$, and $R_{ij}=\overline{u_i'u_j'}$, called the subgrid-scale Leonard, cross, and Reynolds stresses, respectively.

Smagorinsky (1963) was the first to propose a model for the subgrid-scale stresses. His model assumes that they follow a gradient-diffusion process, similar to molecular motion. It is still the most popular algebraic eddy viscosity model, with τ_{ij} given by

$$\tau_{ij}=2\nu_T\bar{S}_{ij},\ \nu_T=\bar{\rho}C_s^2\bar{\Delta}_G^2|\bar{S}| \tag{5}$$

where, ν_T is the subgrid eddy viscosity, C_S is the Smagorinsky constant, $\bar{S}_{ij}$ is the resolved scale strain-rate tensor and $|\bar{S}|=(2\bar{S}_{ij}\bar{S}_{ij})^{1/2}$.

To model the Reynolds subgrid-scale stress tensor, τ_{ij}, deductively that is applicable to the incompressible flow with structured grids, we must consider the quantity $\overline{u_iu_j}-\bar{u}_i\bar{u}_j$. Using the Taylor series expansion for Gaussian filtered quantities, we have

$$\overline{u_iu_j}=\left[\bar{u}_i\bar{u}_j+\frac{\Delta^2}{12}(\nabla\bar{u}_i\cdot\nabla\bar{u}_j)+\frac{1}{2}\left(\frac{\Delta^2}{12}\right)^2(\nabla\nabla\bar{u}_i:\nabla\nabla\bar{u}_j)\right]+\cdots \tag{6}$$

In principle, an exact LES would be found by keeping all terms in the expansion for the deductive model. By keeping all terms, all scales down to the Kolmogorov scale η would be accounted for. Although viscosity may be very large, it is finite and responsible for the final energy dissipation of the system. But at large Reynolds number, as a practical matter, we cannot deal with the dissipation scale directly. So based on the Kolmogorov hypothesis, we make the reasonable assumption of a dynamic similarity, in a statistical sense, between the smallest eddy dictated by viscosity and the smallest eddy allowed by the filter size Δ which presumably lies within the inertial subrange. From experiments we know that if the Reynolds number is large enough, the inertial subrange begins at about 1/3rd the large scale. This is the Smagorinsky model.

Therefore, the truncated deductive model in Eq. (6) treats the eddies immediately below Δ, but not those very small eddies which account for the dissipations. Thus, it seems fair to conclude that we need the Smagorinsky model to describe the dissipation correctly, and the truncated deductive model to ensure a smooth cascade process. A linear combination of deductive model and eddy viscosity model turned out to correlate better with the exact value than the Smagorinsky model alone by Lee and Meecham (1996). But this model may have difficulties due to its inevitable truncation when treating a mixed problem of transition to turbulence, separation, free shear layer, and vortex shedding.

The dynamic subgrid-scale turbulence model was proposed by Germano et al.(1991) to simulate closely the state of the flow by locally calculating the eddy viscosity coefficient through double filtering. This model exhibits the proper asymptotic behavior near boundaries or in laminar flow without requiring damping or intermittency. However, these models with a Gaussian filter are more demanding from the double filtering at each time step in terms of computation

time.

Applying both grid and test filters, G and T to the continuity equation yields

$$\frac{\partial \bar{u}_i}{\partial x_i}=0 \tag{7}$$

Applying both filters, T and G, to the Navier-Stokes equations yields

$$\rho\frac{\partial \bar{u}_i}{\partial t}+\rho\bar{u}_j\frac{\partial(\bar{u}_i)}{\partial x_j}=-\frac{\partial \bar{p}}{\partial x_i}+\mu\nabla^2\bar{u}_i+\frac{\partial T_{ij}}{\partial x_j} \tag{8}$$

The main issue of present modeling is the use of two stress tensors for Gaussian-filtered approach where the SGS stress at the test-filter level is defined as:

$$T_{ij}=-\rho(\overline{\overline{u_iu_j}}-\bar{u}_i\bar{u}_j) \tag{9}$$

Combining the test and grid-filters GT, the algebraic eddy viscosity model, T_{ij} can be assumed as:

$$T_{ij}=2\rho C\Delta_T^2\,|\,\bar{S}\,|\,\bar{S}_{ij} \tag{10}$$

The normalized Gaussian filter in three dimensions is:

$$G(\underline{x}-\underline{z},\,\Delta)=\left(\sqrt{\frac{6}{\pi\Delta^2}}\right)^3 e^{(-6(\underline{x}-\underline{z})^2/\Delta^2)} \tag{11}$$

The grid-filtered variable can be expanded in terms of Taylor series for a Gaussian filter as:

$$\bar{F}(\underline{x})=\left[1+\frac{\Delta_G^2\nabla^2}{24}+\frac{1}{2!}\left(\frac{\Delta_G^2\nabla^2}{24}\right)+\cdots\right]F(\underline{x}) \tag{12}$$

The resolved turbulent stress tensor, L_{ij}, is defined as:

$$L_{ij}=T_{ij}-\overline{\tau_{ij}}=\rho(\bar{u}_i\bar{u}_j-\overline{\bar{u}_i\bar{u}_j}) \tag{13}$$

where the elements of L_{ij} are resolved components of the stress tensor associated with scales of the motion between the test-scale and the grid-scale. We can also define M_{ij} as follows

$$M_{ij}=\rho(\Delta_{GT}^2\,|\,\bar{S}\,|\,\bar{S}_{ij}-\overline{\Delta_G^2\,|\,\bar{S}\,|\,\bar{S}_{ij}}) \tag{14}$$

An attractive property of the explicit Gaussian filter lies on the fact that the commutative product $GT(=TG)$ between the two Gaussian filters of G and T with characteristics lengths of Δ_G and Δ_T gives other Gaussian filter with a characteristic length, Δ_{GT}, given by Germano (1992):

$$\Delta_{GT}^2=\Delta_G^2+\Delta_T^2=\Delta_G^2(r^2+1) \tag{15}$$

Lilly (1992) suggested that the error in C can be minimized by applying a least-square approach to Germano's dynamic procedure:

$$C(x,\,y,\,z,\,t)=\frac{1}{2}\frac{L_{ij}M_{ij}}{M_{ij}M_{ij}} \tag{16}$$

If we apply the Taylor series expansion to test Gaussian-filtered quantities, we have:

$$L_{ij}=\frac{\Delta_T^2}{12}\frac{\partial \bar{u}_i}{\partial x}\frac{\partial \bar{u}_j}{\partial x}-\frac{\Delta_T^4}{24^2}\frac{\partial^2\bar{u}_i}{\partial x^2}\frac{\partial^2\bar{u}_j}{\partial x^2}+\cdots \tag{17}$$

$$\begin{aligned}M_{ij}=&(\Delta_{GT}^2-\Delta_G^2)\,|\,\bar{S}\,|\,\bar{S}_{ij}\\&+\frac{\Delta_T^2(\Delta_{GT}^2-\Delta_G^2)}{24}\left(|\,\bar{S}\,|\frac{\partial^2\bar{S}_{ij}}{\partial x^2}+\bar{S}_{ij}\frac{\partial^2|\,\bar{S}\,|}{\partial x^2}\right)\\&+\Delta_{GT}^2\left(\frac{\Delta_T^2}{24}\right)^2\frac{\partial^2|\,\bar{S}\,|}{\partial x^2}\frac{\partial^2\bar{S}_{ij}}{\partial x^2}\\&-\frac{\Delta_G^2\Delta_T^2}{12}\frac{\partial|\,\bar{S}\,|}{\partial x}\frac{\partial\bar{S}_{ij}}{\partial x}+\cdots\end{aligned} \tag{18}$$

A priori test on a direct numerical simulation of fully developed pipe flow was done to evaluate this approach by Brun et al.(2001), and showed that such a formulation highly increased the correlations between real stress tensors from DNS and modelled tensors.

The turbulent eddy viscosity using dynamic Smagorinsky constant is now determined as:

$$\nu_T=C\bar{\Delta}^2\,|\,\bar{S}\,| \tag{19}$$

The dynamic Smagorinsky constant, C, obtained deductively by using Eqs. (16)-(18) was tested and applied to solve the subgrid-scale stress tensor in Eqs. (5). This SGS model does not need an averaging in a homogeneous direction for smoothing which has usually prevented the dynamic model from being applied to the flows of complex geometry e.g. turbomachinery impeller (Lee et al., 2003).

2.2 Numerical method and boundary conditions

The numerical simulation of an unsteady, turbulent flow through a cascade of blades was performed with the modified ANSWER code (Runchal and Batia, 1993), which accommodates the subgrid-scale model proposed by Lee and Meecham (1992) for LES computation.

The collocated arrangement is used with Cartesian velocity components of finite volume approach as shown in Fig. 1. In general, the flux is computed from Green's theorem as

$$\frac{\partial\phi}{\partial x_i}=\frac{1}{V}\int_S \phi\vec{S}\cdot\vec{i}_x \tag{20}$$

For computing fluxes, we also require the gradients at the faces, say, $\partial p/\partial x\,|_e$. If we determine $\partial p/\partial x\,|_e$ as a linear interpolation of $\partial p/\partial x\,|_p$ and $\partial p/\partial x\,|_E$, then it can be seen that the direct effect of nodes P and E will be reduced and effects of nodes ee and w will enter the formula. This is not desirable either from the numerical standpoint or from computational convenience.

There are a number of alternative ways in which $\partial p/\partial x\,|_e$ can be determined. The simplest is to define a closed surface extending from node E to node P with other surfaces between these in the y and z directions. The most general approach is to define $\partial p/\partial x\,|_e$ on both sides of the e surface as given below and then interpolate.

$$\left.\frac{\partial\phi}{\partial x}\right|_e^+=\frac{1}{V_e^+}\{A_E\phi_E-A_e\phi_e +\beta^+[A_{ne}\phi_{ne}-A_{se}\phi_{se}+A_{ue}\phi_{ue}-A_{de}\phi_{de}]\} \tag{21}$$

where, β^+ is the fraction of the total surface which is contained between the e-E connection. We have for simplicity assumed that β^+ for all surfaces is constant, though in reality it will vary. But for all practical purposes, this choice of constant β^+ should suffice since, in any case, $\partial\phi/\partial x\,|_e$ is being obtained from linear interpolation. Further, consistent with the assumption, we shall also assume that

$$V_e^+=\beta^+V_E,\quad A_E=A_e+\beta^+(A_{ee}-A_e) \tag{22}$$

so that Eq. (21) is now written as

$$\left.\frac{\partial\phi}{\partial x}\right|_e^+=\frac{A_e}{V_e^+}(\phi_E-\phi_e)+\left.\frac{\partial\phi}{\partial x}\right|_E +\frac{1}{V_E}\{(A_{ee}-A_e)\phi_E-A_{ee}\phi_{ee}+A_e\phi_e\} \tag{23}$$

In the same way, we now write $\partial\phi/\partial x\,|_e^-$ as

$$\left.\frac{\partial\phi}{\partial x}\right|_e^-=\frac{A_e}{V_e^-}(\phi_e-\phi_P)+\left.\frac{\partial\phi}{\partial x}\right|_P +\frac{1}{V_P}\{(A_e-A_w)\phi_P-A_e\phi_e+A_w\phi_w\} \tag{24}$$

Now $\partial p/\partial x\,|_e$ can be obtained by linear interpolation as

$$\left.\frac{\partial\phi}{\partial x}\right|_e=\gamma\left.\frac{\partial\phi}{\partial x}\right|_e^-+(1-\gamma)\left.\frac{\partial\phi}{\partial x}\right|_e^+ \tag{25}$$

where $\gamma=\alpha_{eE}/\alpha_{PE}$ and α is the distance.

With the same level of interpolation accuracy, we may write

$$\gamma=\frac{V_e^+}{V_e};\ 1-\gamma=\frac{V_e^-}{V_e},\ V_e=V_e^+V_e^- \tag{26}$$

Now we may write

$$\left.\frac{\partial\phi}{\partial x}\right|_e=\frac{A_e}{V_e}(\phi_E-\phi_P)+\frac{V_e^+}{V_e}\left.\frac{\partial\phi}{\partial x}\right|_P +\frac{V_e^-}{V_e}\left.\frac{\partial\phi}{\partial x}\right|_E+\frac{S_\phi}{V_e} \tag{27}$$

where,

$$S_\phi=\frac{V_e^+}{V_P}A_w\phi_w-\frac{V_e^-}{V_E}A_{ee}\phi_{ee} +\left(\frac{V_e^+}{V_e^-}-\frac{V_e^-}{V_e^+}+\frac{V_e^-}{V_E}-\frac{V_e^+}{V_P}\right)A_e\phi_e +\left(A_e\frac{V_e^-}{V_e^+}-A_e+A_{ee}\frac{V_e^-}{V_E}-A_e\frac{V_e^-}{V_E}\right)\phi_E +\left(A_e-A_e\frac{V_e^+}{V_e^-}+A_e\frac{V_e^+}{V_P}-A_w\frac{V_e^+}{V_P}\right)\phi_E$$

The equation of continuity was transformed into an equation for computation of the density in this study. This approach of working directly with the density variable is termed DEFCON for Density Equation Formulation of Continuity

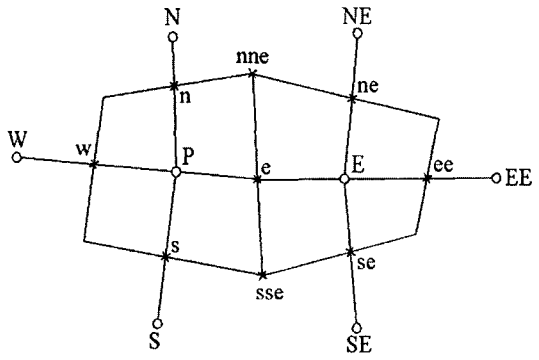

Fig. 1 Collocated grid arrangement

equation. The governing Navier-Stokes equations are integrated by Finite Volume Method (FVM) for a collocated, structured grid system. A major advantage of this method is that it intrinsically preserves the mass, material fluxes both on local and global scales. The numerical integration starts with the assumption of an integration profile for the state variable. The CONDIF (Runchal, 1987) scheme, which is stable and second order accurate, is employed in this research. In this work, the Alternating Direction Implicit (ADI) solution was used, which solves the set of algebraic equations in three sweeping directions. This temporal discretization of the ADI method is proven to be unconditionally stable in a linear sense. But it may not be accurate in time if the time step is large due to the neglecting of the third-order term that is essential to the factorization.

2.3 Flow condition and grid test

Simulation of the flow past a cascade was carried out to explore the flow feature in the cascade both at design and off-design conditions. Physical dimensions and blade angles of the cascade are depicted in Fig. 2. In the cascade, the solidity is 1.43 and the blade height is 20 cm. Simulations were performed at seven incidence angles including the design condition in which the incidence angle is zero. In all cases, the flow coefficient was kept the same by varying incoming velocity as shown in Table 1.

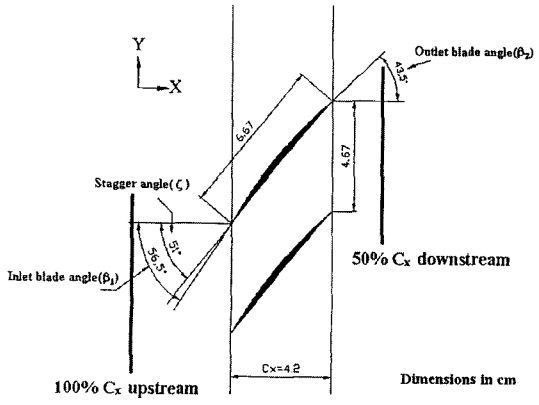

Fig. 2 Schematic of the cascade

In the simulation, flow and acoustic fields are calculated simultaneously. The numbers of the H-type grids in x-, y-, and z-directions are $362\times168\times3$, $362\times334\times3$, $362\times168\times12$, $362\times168\times24$ for 2-D computation with two blades (2D2B domain), 2-D computation with four blades (2D4B domain), and 3-D computation with two blades (3D2B domain) in each computational domain, respectively. The cases of 2D4B domain and 3D2B domain are tested to see the pitch-wise and span-wise variations of shedding pattern for incidence angles of $+5°$ and $+10°$. The inlet boundary is placed at an upstream location of 8 times C_x, while the outlet boundary is placed at a downstream location of 10 times C_x. On the outlet boundary, the convective boundary conditions of Hayder et al.(1995) were used to make the boundary non-reflective. The periodic boundary conditions were used on boundaries in

Table 1 Inlet conditions at each incidence angle

Incidence angle (°)	Velocity (m/s)	Re_C
20	29.4	1.30×10^5
10	31.5	1.39×10^5
5	30.4	1.34×10^5
0	27.6	1.20×10^5
−10	26.1	1.15×10^5
−20	20.1	8.84×10^4
−40	16.7	7.20×10^4

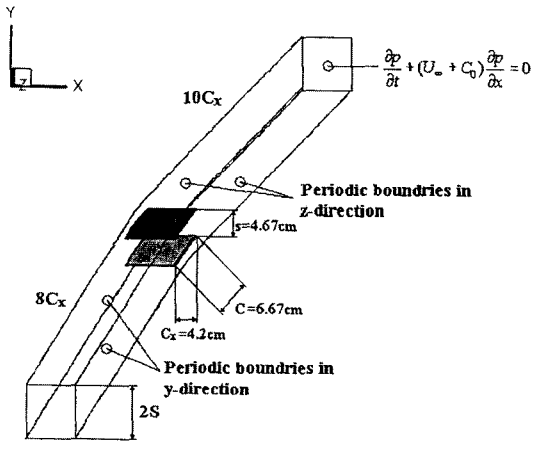

Fig. 3 Computational domain for flows over cascade

Table 2 Lift and drag coefficients at each case of grid numbers

Grid no.(x-y-z)	C_D	C_L
242-112-3	0.056	0.343
242-112-12	0.054	0.343
242-112-24	0.055	0.344
362-168-3	0.055	0.330
362-168-12	0.053	0.329
362-168-24	0.054	0.331
542-248-3	0.053	0.316

pitch-wise and span-wise directions for each computational domain as shown in Fig. 3. The non-dimensional time step ($\Delta t \cdot U_\infty / C_o$) in the present simulation ranged from 23,000 to 50,000 with the maximum CFL number of 0.27.

The numerical data have been compared against experimental results (Hong et al., 2002) which were acquired at 100% axial chord length upstream from the leading edge of the blades, and 50% axial chord length downstream from the blades' trailing edge.

To establish the grid-independency of the code, the cases having different grid numbers as shown in Table 2 were also tested at an incidence angle of $+5°$. The time-mean values of C_D and C_L computed from surface pressures were found to remain almost constant by increasing the grid numbers from 3 to 24 in the spanwise direction as given in Table 2. Doubling the grid numbers approximately in both x and y directions caused the time-mean values of C_D and C_L to be reduced by 5 and 8 percents, respectively. The time-mean values of C_D and C_L are more influenced by the in-plane grid number than the spanwise grid number. This test ensures that the two-dimensional phenomenon is dominant in a cascade flow. While the time-mean lift coefficients do not differ from each other for the cases of 2D and 3D simulation, but their amplitudes differ very significantly. The time history of fluctuating lift coefficient will be discussed in the section 4.2.

To assess the feasibility of spanwise grid numbers, two cases of 362×168×12 and 362×168×24 are tested and compared in Fig. 4. The case of 24 grids in spanwise direction are found to resolve the quasi-periodic pattern near T.E. more clearly, nevertheless the time-mean values of C_D and C_L remain almost constant. The values of C_D and C_L for the cases of 362×168×12 and 362×168×24 are 0.053 and 0.329, 0.054 and 0.331, respectively. The spanwise resolution is considered to help the unsteady amplitude of dipole source functions and spanwise coherency near T.E. to be more physically described.

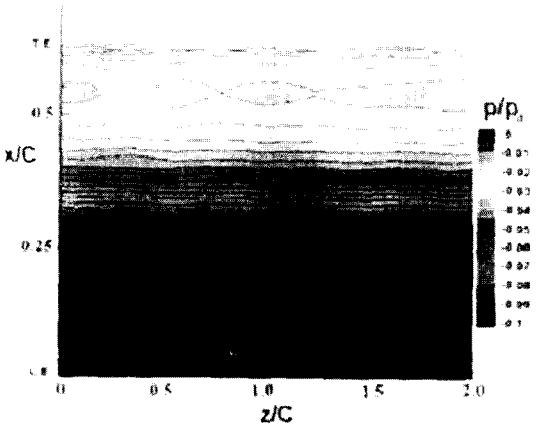

(a) Spanwise grid number of 12

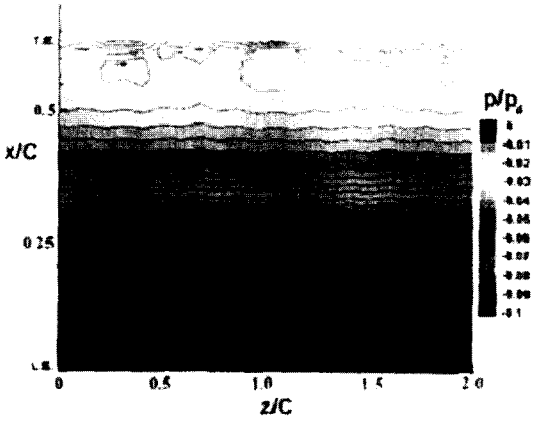

(b) Spanwise grid number of 24

Fig. 4 Non-dimensional surface pressure contours on suction side for the cases of 12 and 24 spanwise grid numbers

3. Experimental Facilities

The noise experiments were conducted in an anechoic wind tunnel with an open test section

that measures 40 cm wide and 40 cm high, and the maximum speed at the test section is 30 m/s. The maximum value of turbulence intensity on the order of 0.25% and total pressure variations on the order of 0.2% were measured and considered adequate to prevent any spurious effects on aerodynamic coefficients. A more detailed description of the wind tunnel is in Lee et al.(2000).

A cascade composed of identical blades is mounted on a turning table and placed downstream of the contraction of the tunnel. In this set-up, the cascade was composed of only four blades for an exact comparison with numerical data and had the free-stream to pass through the mid-span by having the jet efflux height of 14 cm by an contraction to get rid of any effect by horseshoe vortex near the junction of wall and blades. The side walls were also removed so as not to accelerate the flow in the passage near the side wall, which was believed to create more discrete sound before.

The turning table is a semicircular disk made of 8mm thick plexiglass. An adapter was placed between the exit of the wind tunnel test section and the inlet of the cascade to make all air pass through the cascade. The stagger angle was kept at 51° and only the incidence angle was varied from −40° to 20° by rotating the turning table. Thus, the effect of the stagger angle was not explored in the present research even though its effect on the performance of a cascade is significant as Yocum and O'Brien (1993) claimed. The blade is a double circular airfoil with blade height of 20 cm. The dimensions of the blade and cascade are depicted in Fig. 2. The aerodynamic performance of the same cascade was measured in an open-type wind tunnel. These experimental results are discussed in detail in a companion paper by Hong and Song (2002).

The incidence angle was varied from −40° to 20° and the velocity was adjusted to keep the axial velocity constant regardless of the incidence angle as shown in Table 1. The Reynolds numbers based on free-stream velocity (U_∞) and blade chord length (C) ranged from 7.2×10^4 to 1.39×10^5. Laminar flows with laminar separation bubbles are often encountered in the blade

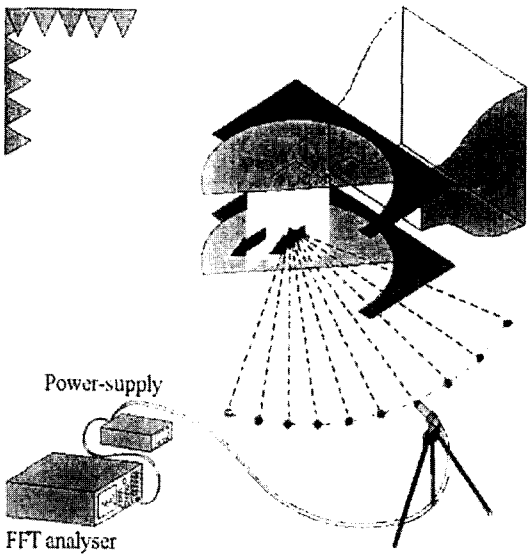

Fig. 5 Experimental setup for far-field noise measurements

cascade at Reynolds numbers less than 2×10^5. This separation bubble will reattach and may initiate transition resulting in turbulent flow downstream.

Far-field sound measurements were carried out by using a 1/2″ B&K Model 4189 microphone, which was traversed by 10 degrees circumferentially to measure noise directivity patterns from the cascade for the conditions described as in Table 1. The distance from the center of the cascade to the tip of the microphone was kept 1 meter as depicted in Fig. 5. Radiated sound pressure levels were acquired by using a 2-Ch FFT analyzer (Stanford Research Model SR780). The sound pressure level at each measuring location was calculated from the ensemble-averaged spectrum of 1,000 short-time spectra.

4. Results and Discussion

4.1 Simulated flow patterns

The simulated flow-fields in the 2D2B domain for the incidence angle of −20° at four time steps are shown in Fig. 6. In the figure, the time steps are represented in terms of the period of vortex formation and decay on the blade. The flow on the pressure side was separated near the leading

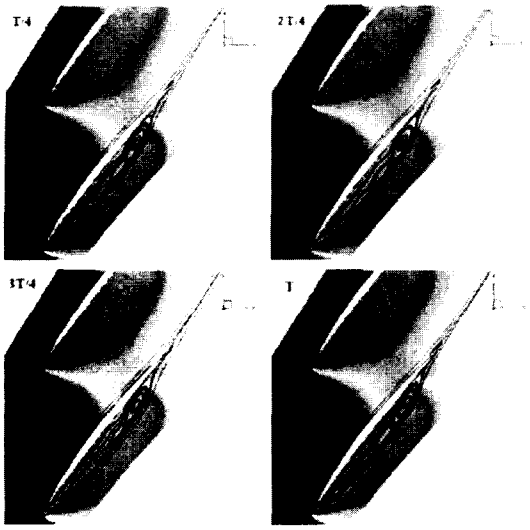

Fig. 6 Streamline patterns at t=T4~T in one period (incidence angle −20°; 2D2B model)

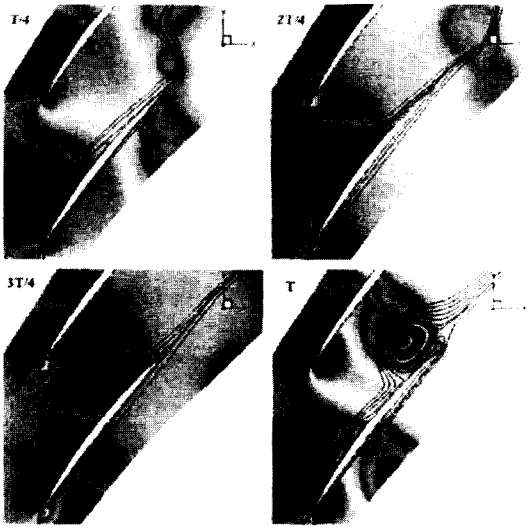

Fig. 8 Streamline patterns at t=T4~T in one period (incidence angle +20°; 2D2B model)

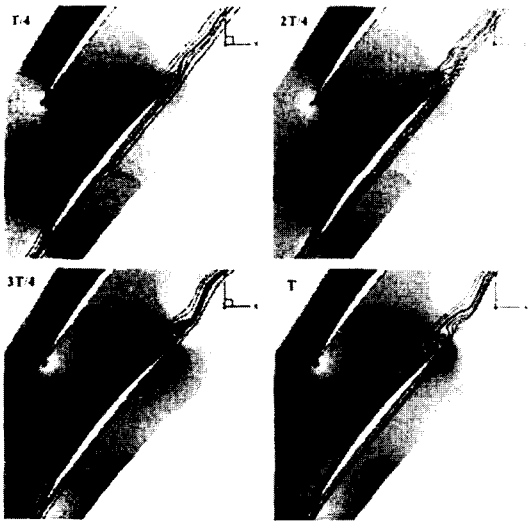

Fig. 7 Streamline patterns at t=T4~T in one period (incidence angle 0°; 2D2B model)

edge due to high negative incidence angle. Several co-rotating separation bubbles are observed in the separated region as shown in the figure. However, a wake was not developed downstream of the blade or cascade, and thus the separation would not cause any serious problem as in the case of positive incidence angles. Shown in Fig. 7 are the instantaneous flow patterns at an incidence angle of 0°. The streamlines just downstream of the trailing edge seem to oscillate with a phase angle in the normal direction of the flow direction. Although this oscillation is not too significant, it probably alters dynamic pressure at a downstream location. For the case of an incidence angle of +20°, the separation bubble formed at the leading edge travels downstream and grows in size with increasing downstream location as shown in Fig. 8. This enlarged and unsteady vortex will reduce the effective flow passage and in turn result in stall.

4.2 Aerodynamic performance of the cascade

The simulated results were compared with experimental results to see if the use of LES to predict the performance of a cascade is applicable to separated/stalled flows. The pressure loss coefficient, defined as

$$C_{p_t}=\frac{p_{t_1}-p_{t_2}}{\rho v_1^2/2} \tag{28}$$

is shown in Figs. 9 and 10 for incidence angles of 5° and −40°, respectively. For the case of an incidence angle of 5°, the predicted/simulated total pressure loss coefficient compares fairly well with the experimental results except the downstream of the suction side of the blade. The coefficients showed some difference at an incidence angle of −40° as shown in Fig. 10. How-

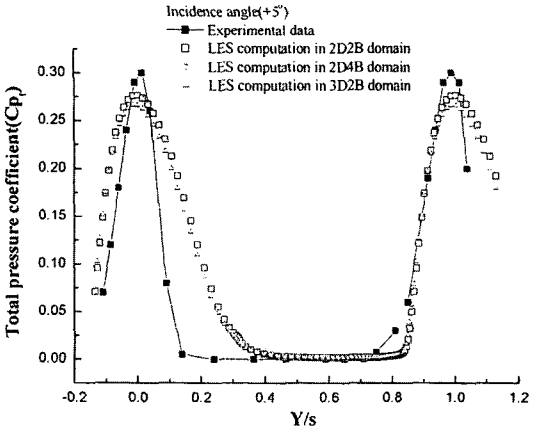

Fig. 9 Distribution of total pressure coefficients along pitch-wise direction at an incidence angle of +5°

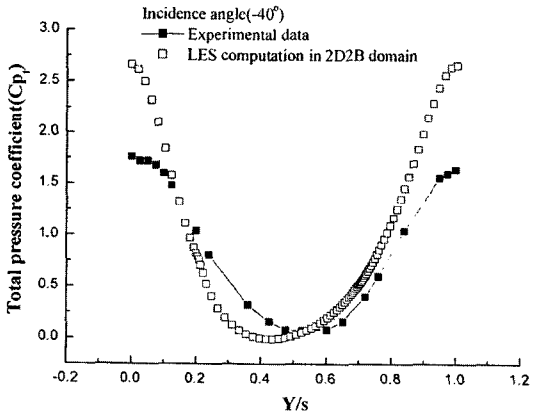

Fig. 10 Distribution of total pressure coefficients along pitch-wise direction at an incidence angle of −40° (2D2B model)

ever, the trend of total pressure coefficients for both cases was well predicted.

The total pressure loss coefficient and deflection angles with incidence angle are shown in Fig. 11. The total pressure loss coefficient (ω) is defined as:

$$\omega=\frac{p_{t_1}-p_t}{p_{t_1}-p_1}=\frac{\Delta p_o}{\rho v_1^2/2}=\frac{\int_s^0 \rho v_x C_{Pt} dy}{\int_s^0 \rho v_x dy} \tag{29}$$

The deflection angle is the difference of flow angles at inlet and outlet of the cascade. The vertical dotted line represents the onset incidence

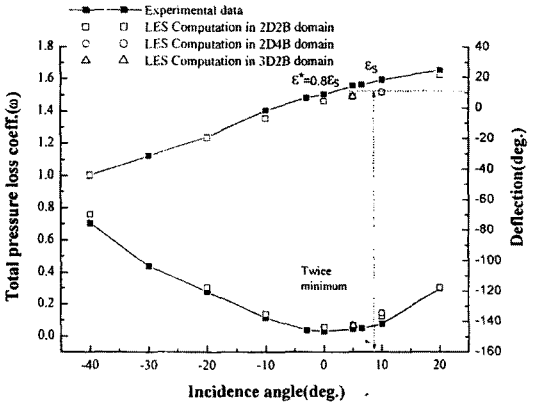

Fig. 11 Cascade mean deflection and pressure loss curve by LES computation with those by experiment

angle of stall for experimental data. In general, the onset incidence angle of stall is decided at a point where the total pressure loss coefficient is twice the minimum value. Based on this, the measured and simulated stall-onset incidence angles are found to be, respectively, 7.1° and 12.8°. According to Howell (1942), the deflection angle at the nominal condition is defined as 80% of the maximum deflection angle. The measured and simulated deflection angles at the nominal condition are given as 13° and 8.6°, respectively.

Transitional flow may depend on inlet turbulence levels, pressure gradients, and Reynolds number. Depending on inlet turbulence intensity, the transition may commence at a Reynolds number of 1×10^5 based on chordwise location (Lee and Kang, 2000). The measured cases in the range of incidence angle greater than −10° and less than 10° may be considered to have transitions at streamwise locations of about 80% of blade chord while the predicted cases may not have any transition on the blade due to no turbulence fed at the inlet of computational domains at the Reynolds numbers considered.

The drag and lift coefficients are shown in Fig. 12, and they may be defined as:

$$C_D=\frac{D}{\rho U_\infty^2 C/2}=\frac{\Delta p_o}{\rho v_1^2/2}\frac{s}{C}\frac{\cos^3\beta_\infty^*}{\cos^2\beta_1^*}=\frac{\omega}{\sigma}\frac{\cos^3\beta_\infty^*}{\cos^2\beta_1} \tag{30}$$

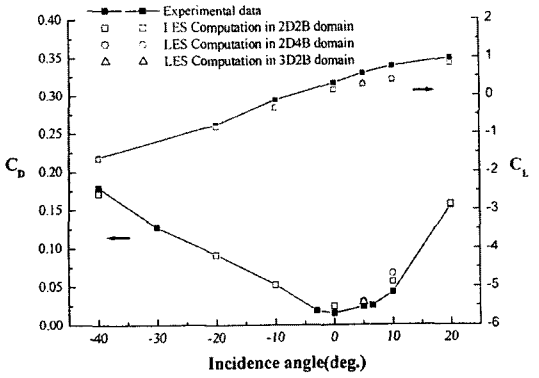

Fig. 12 Comparison of drag and lift coefficient by LES computation with those by experiment

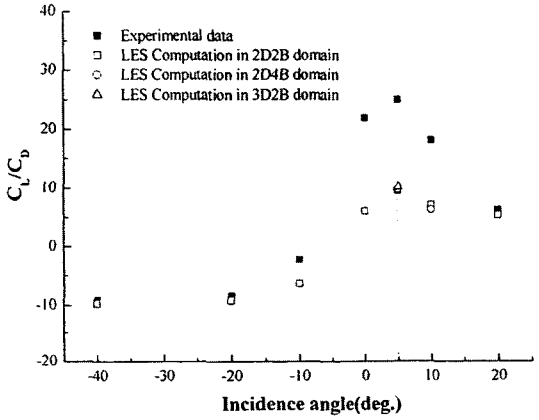

Fig. 13 Comparison of lift-drag ratios by LES computation with those by experiment

$$C_L=\frac{2}{\sigma}[\tan\beta_1^*-\tan\beta_2^*]\cos\beta_\infty^* - C_D\tan\beta_2^* \tag{31}$$

The predicted values of both coefficients well agree with the measured data. Since the drag coefficient is proportional to the total pressure loss coefficient and other parameters are given as shown in Fig. 12, one may calculate the onset incidence angle of stall at a point where the drag coefficient is double the minimum drag coefficient. In fact, this is the approach Carter (1950) used to define the onset incidence angle of stall. For an incidence angle greater than the measured or predicted onset angle, which is about 10° as mentioned before, the drag coefficient increased rapidly with increasing incidence angle as observed in Fig. 12. Shown in Fig. 13 are ratios

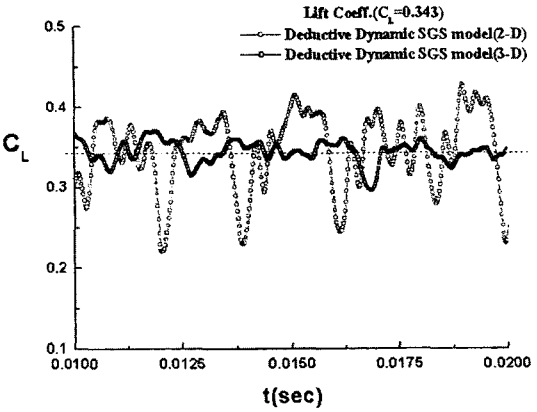

Fig. 14 Time history of lift coefficients by 2-D and 3-D LES at an incidence angle of +5°

between drag and lift coefficients. If one uses Carter's (1950) method to decide the optimum condition of maximum lift-drag ratio, the optimal incidence angles seem to coincide with each other for measured and predicted cases.

Figure 14 shows the time history of lift coefficients predicted by 2D and 3D LES simulations by using the deductive dynamic SGS model at an incidence angle of 5°. The time-mean lift coefficients were found 0.343 for both cases, but their amplitudes differed from each other very significantly because 2D simulation usually leads to exaggerated vorticity fields for unsteady cases. The dynamic behaviors by 3D simulation are found to be more suppressed than 2D case, but the steady-state values remain the same, which is common in the cascade analysis.

4.3 Flow-Induced noise from the cascade

A hybrid method using acoustic analogy was employed to compute the far-field sound and directivity patterns from the separated vortex with or without shedding at off-design points of the blade cascade. For a continuous force field of density F_i the sound field is given by an integral over the region of flow containing the force field,

$$4\pi p'(\vec{x},\ t)=-\frac{\partial}{\partial x_i}\int_V[F_i]\frac{dV(\vec{y})}{r} \tag{32}$$

If the space derivative is evaluated and the near field neglected, equation (19) reduces to

$$4\pi p'(\vec{x}, t) = -\frac{1}{C_0}\int_S \int \frac{x_i - y_i}{r^2}\left[\frac{\partial F_i}{\partial t}\right] dS(\vec{y}) \quad (33)$$

While Ffowcs Williams and Hall's theory (1970) offers acoustic scatterings and reflections of turbulence over an infinite half plane by involving an acoustic Green's function, this approach does not take into account the possible acoustic reflections on the airfoil walls. But it is not feasible to find an appropriate acoustic Green's function for this complex geometry unless a numerical Green' s function is introduced by using the boundary element method. No such work has been reported to the author's best knowledge.

Far field radiated sound from the blade was computed using the time-dependent flow field as described earlier, for the full range of radiation angles in 10° increments at 10 meters (R) from the center of blade chord. Radiation angle is defined such that 90° is along the mean relative velocity vector W_∞. A fifth-order polynomial regression was applied to find time-derivatives of surface force densities at each retarded time by using non-dimensional time interval $(C_o \cdot \Delta t/R)$ of 6.8×10^{-5}. Overall Sound Pressure Level (OASPL) was calculated after averaging sound pressures obtained from more than 200 realizations, and normalized to a reference radius of one meter for comparison.

In Fig. 15, the noise amplitudes are compared between experimental values and those by deductive and deductive dynamic models at an incidence angle of 5°. The sound pressure levels from the dipole sources on the blade underestimated the experimental values by both deductive and deductive dynamic SGS models, but the dynamic one resulted in more accurate SPL's than the deductive one. The 2D dynamic model overpredicts the noise from cascade by more than 10 decibels at the maximum radiation angle. All the directivity patterns by three models deviates from the measured one in the same way because all cases assumed that the surface pressures on each blade are uncorrelated enough to add its contribution to the OASPL's separately by using the simple relation of $10\,\mathrm{Log}_{10}(n)$ where n is the number of blades. But in real situation, the displaced

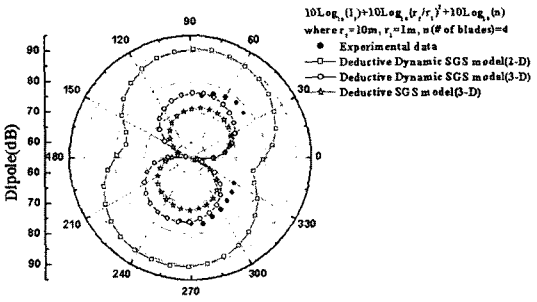

Fig. 15 Directivity patterns of far-field sound pressure levels at an incidence angle of +5°

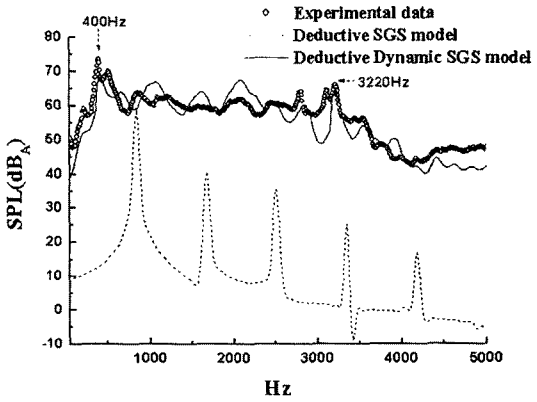

Fig. 16 Power spectra of far-field sound at an incidence angle of +5°

arrangement of blades having uncorrelated source fields affects the near-fields together with quadrupole sources, resulting in the deviation from the compact dipole distribution.

The computed sound energy spectrums are compared with the measured noise spectrum, as shown in Fig. 16, at an incidence angle of 5° for deductive model and deductive dynamic model. The measured one shows the characteristics of typical turbulent boundary layer noise of broadband with a few narrow-band peaks at 400 and 3,220 Hz, which are closely related to oscillating vortices inside the separation bubble and the shedding vortices near T.E., respectively. Both models can predict the overall sound power level and directivity pattern from the cascade flow within a specified accuracy. But the deductive model only captures the discrete frequency characteristics while the deductive dynamic model

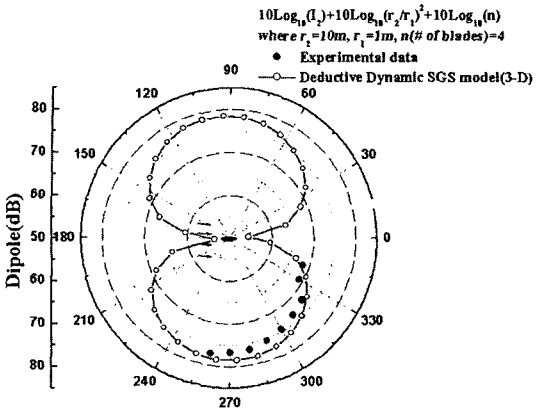

Fig. 17 Directivity patterns of far-field sound pressure levels at an incidence angle of $-10°$

helps to depict the real sound in the spectral sense.

Comparisons of measured and simulated OASPL's versus radiation angle are also made in Fig. 17 for an incidence angle of $-10°$. The simulated result using the deductive dynamic model for an incidence angle of $-10°$ is in excellent agreement with the measured data except the slight over-prediction near the maximum radiation angle as seen in Fig. 17. The measured directivity pattern of dipole characteristic for the incidence angle of $-10°$ has a maximum radiation at 10 degrees deviated from the lift force direction, along which the simulated one has its maximum.

5. Conclusions

An efficient fluid dynamics model for time-dependent, two- and three-dimensional representations of turbulent flows in a compressor cascade and far-field radiation from it has been developed, incorporating large-eddy simulation and Lighthill's acoustic analogy.

The subgrid-scale models employed use a hybrid of Smagorinsky's model and mathematical deduction in two ways of simple truncation and dynamic approach. The unsteady, turbulent flows with incidence angles ranging from $-40°$ to $+20°$ have been computed. The oscillating separation bubbles attached to the suction surface do not modify wake flows dynamically for negative incidence angles. Simulated characteristics follow trends of experimental data for all cases and show some deviations for the non-extreme incidence angles, e.g., between $-10°$ and $+10°$ where the natural transition must be accounted by simulation for the Reynolds numbers of concern. An incidence angle greater than $+8°$ caused a separated vortex near the leading edge to be shed downstream and created stalling. The separated vortices in each passage do not occur simultaneously and show the typical mode of rotating instability at large incidence angles.

Computed far-field noise levels and directivity patterns are in close agreement with those measured at specified conditions in anechoic wind-tunnel facility. While the off-design case of a negative incidence angle shows dipole source characteristics, the measured case of a positive incidence angle exhibits a directivity pattern with not negligible contribution of quadrupole sources, which suggests subsequent research on volume sound effects at least for stalling.

References

Brun, C. and Friedrich R., 2001, "Modeling the Test SGS Tensor T_{ij}: An Issue in Dynamic Approach," *Physics of Fluids*, Vol. 13, pp. 2373~2385.

Carter, A. D. S., 1950, "Low Speed Performance of Related Aerofoils in Cascade," ARC CP, No. 29.

Cornell, W., 1954, "The Stall Performance of Cascades," *Proceedings of 2nd National Conference of Applied Mechanics*, ASME, New York.

Ffowcs Williams, J. E. and Hall, L. H., 1970, "Aerodynamic Sound Generated by Turbulent Flow in the Vicinity of a Scattering Half Plane," *Journal of Fluid Mechanics*, Vol. 40, pp. 657~670.

Germano, M., 1992, "Turbulence: The Filtering Approach," *Journal of Fluid Mechanics*, Vol. 238, pp. 325~336.

Germano, M., Piomelli, U., Moin, P. and Cabot, W. H., 1991, "A Dynamic Subgrid Scale Eddy Viscosity Model," *Physics of Fluids A*, Vol.

3, No. 7, pp. 1760~1765.

Hah, C., 1985, "Modeling of Turbulent Flowfields Through a Cascade of Airfoils at Stall Conditions," *AIAA Journal*, Vol. 23, No. 9, pp. 1411~1417.

Hayder, M. E. and Turkel, E., 1995, "Non-reflecting Boundary Conditions for Jet Flow Computations," *AIAA Journal*, Vol. 33, No. 12, pp. 2264~2270.

Hong, K. R., Song, S. J. and Lee, S., 2002, "Large Incidence Effects on Axial Compressor Cascade Performance," *submitted to the AIAA Journal*.

Howell, A. R., 1942, "The Present Basis of Axial Flow Compressor Design, Part I. Theory and Performance," ARC R. and M. 2095.

Johnsen, I. A. and Bullock, R. O., 1965, "Aerodynamic Design of Axial Flow Compressor," NASA SP-36.

Lee, H. and Kang, S.-H., 2000, "Flow Characteristics of Transitional Boundary Layers on an Airfoil in Wakes," *Journal of Fluids Engineering*, Vol. 122, pp. 522~532.

Lee, S. and Meecham, W. C., 1996, "Computation of Noise from Homogeneous Turbulence and a Free Jet," *International Journal Acoustics and Vibration*, Vol. 1, pp. 35~47.

Lee, S. and Meecham, W. C., 1992, "A Computation of Turbulent Flow Field for a Square Jet and a Far field aerosound using Large-Eddy Simulation," *Bulletin of the American Physical Society*, Vol. 37(8), p. 1796.

Lee, S., Kim, H.-J. and Runchal, A. K., 2003, "Large Eddy Simulation of Unsteady Flow in Turbomachinary," *submitted to the Journal Power and Energy*.

Lee, S., Kim, H.-J., Kwon, O.-S. and Lee, S.-K., 2000, "Wall Pressure Fluctuations and radiated Sound from Turbulent Boundary Layer on an Axisymmetric Body," *Acoustical Society America ARLO*, Vol. 1(1), pp. 7~12.

Lieblien, S., 1965, "Experimental Flow in Two-Dimensional Cascades," Aerodynamic Design of Axial-flow Compressors, NASA SP-36, pp. 183~226.

Lilly, D. K., 1992, "A Proposed Modification of the Germano Subgrid-Scale Closure Method," *Physics of Fluids*, Vol. 4, No. 3, pp. 633~635.

Runchal, A. K. and Bhatia, S. K., 1993, "ASME Benchmark Study: ANSWER Predictions for Backward Facing Step and Lid-driven Cubical Cavity," FED-Vol. 160, ASME, pp. 43~54.

Runchal, A. K., 1987, "CONDIF: A Modified Central-Difference Scheme for Convective Flows," *International Journal Numerical Methods in Engineering*, Vol. 24, pp. 1593~1608.

Smagorinsky, J., 1963, "General Circulation Experiments with the Primitive Equations, Part I: the Basic Experiment," *Monthly Weather Rev.*, Vol. 91, pp. 99~164.

Sovran, G., 1959, "The Measured and Visualized Behavior of Rotating Stall in an Axial-Flow Compressor and in a Two-Dimensional Cascade," *Transaction of the ASME*, Vol. 81, pp. 24~34.

Yocum, A. M. and O'Brien, W. F., 1993, "Separated Flow in a Low-Speed Two-Dimensional Cascade: Part I-Flow Visualization and Time-Mean Velocity Measurements," *Journal of Turbomachinery*, Vol. 115, pp. 409~420.